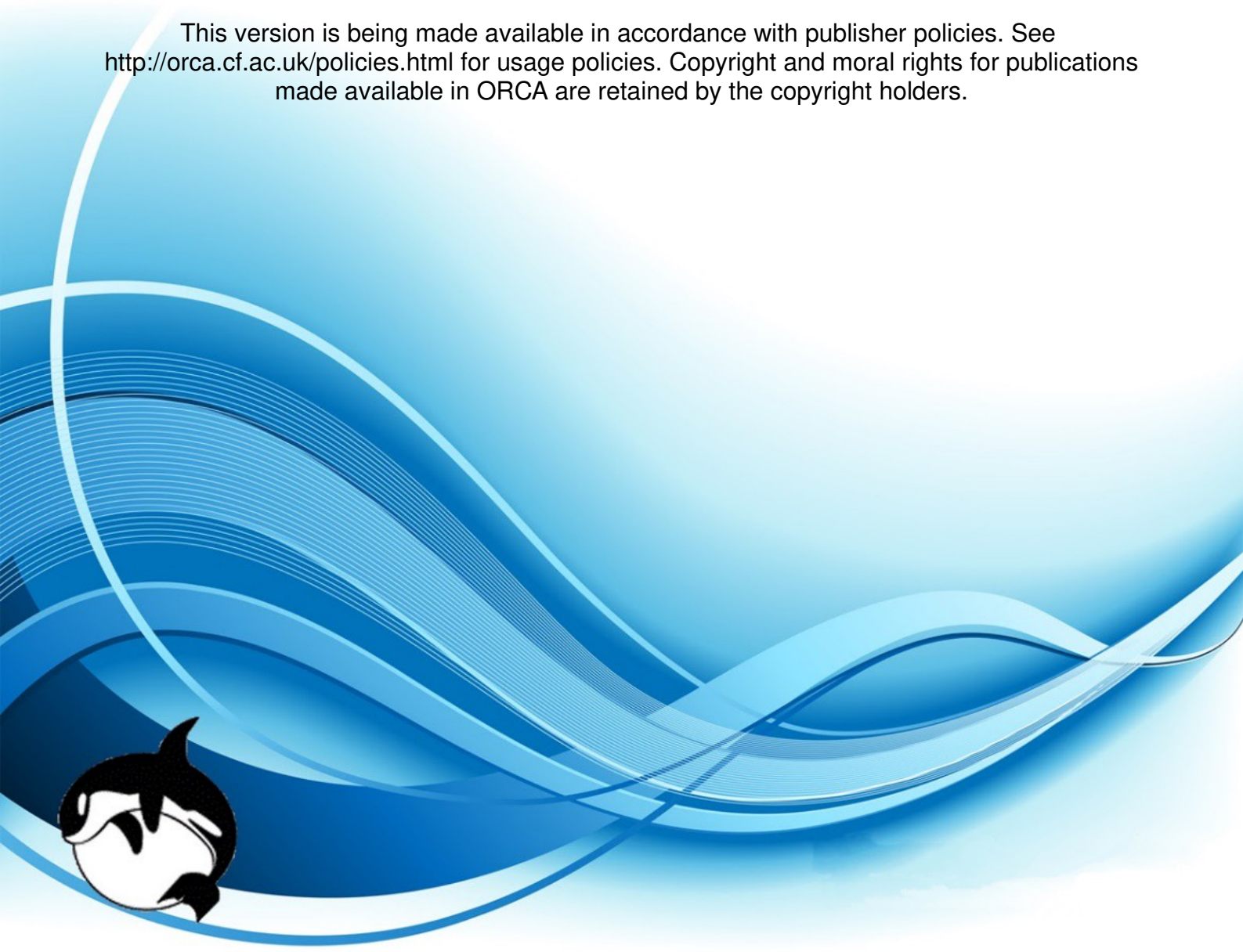

Robust Stochastic Optimal Dispatching of Integrated Electricity-Gas-Heat Systems With Improved Integrated Demand Response

Hongwei LI[a], Hongpeng LIU[a,*], Jianwei MA[b], Yue ZHOU[c], Tao MENG[d].

[a]*The Key Laboratory of Modern Power System Simulation and Control & Renewable Energy Technology, Ministry of Education, Northeast Electric Power University, Jilin 132012, Jilin province, China*
[b]*The Marketing Department, State Grid Corporation of China, Beijing 100031, China.*
[c]*The School of Engineering, Cardiff University, Queen's Building, The Parade, Cardiff CF24 3AA, UK.*
[d]*The State Grid Jilin Electric Power Co., Ltd. Electric Power Science Research Institute, Changchun 130000, Jilin Province, China*

Abstract

In recent years, integrated energy systems with deep coupling of power, natural gas, and heat energy have gradually attracted extensive attention. The increasing issue of uncertainty in the generation and load of an integrated electric-gas-heat system (IEGHS) is a growing prominent problem. The effective implementation of demand response (DR) programs is an important way to solve this problem in the IEGHS. In this paper, a robust stochastic optimal dispatching method for an IEGHS with integrated DR (IDR) under multiple uncertainties is proposed. A robust adjustable uncertainty set is adopted to deal with the uncertainty of wind power. The Wasserstein generative adversarial network based on gradient normalization is proposed to generate load-side demand scenarios. Furthermore, an improved IDR model that considers the peak-valley difference cost of the electricity-gas-heat load is proposed. Finally, the simulation analysis successfully demonstrates the efficacy of the proposed model. By utilizing this approach, the system can obtain a scheduling scheme with the lowest operating cost even under worst-case scenarios.

Keywords: generative adversarial networks, integrated electric-gas-heat system, integrated demand response, multiple uncertainties, robust stochastic optimal dispatching.

Nomenclature

Abbreviations

IEGHS	Integrated electric-gas-heat system
DR	Demand response
SO	Stochastic optimization
RO	Robust optimization
IDR	Integrated demand response
GAN	Generative adversarial network
C&CG	Column and constraint generation
DHN	Distinct heating network

* Corresponding author. E-mail.: liu_hp@neepu.edu.cn.
E-mail address: lihongwei091611@163.com; liu_hp@neepu.edu.cn; 13701305110@139.com; ZhouY68@cardiff.ac.uk; 494344848@qq.com.
http://dx.doi.org/10.1016/xxxxxx
0142-0615 /

http://dx.doi.org/10.1016/xxxx

NG	Natural gas
PMV	Predicted mean vote
GN	Gradient normalization
IDB	Index of Davies-Bouldin
RSOD	Robust stochastic optimal dispatching
CON	Conventional thermal power
CHP	Combined heat and power
EB	Electric boiler
HSS	Heat storage system
PS	Pumped storage
P2G	Power to gas
GS	Gas storage
IIDR	Improved integrated demand response

Parameters

$m_{s,t}^{\mathrm{G}}$	Mass flow rate of heat source s at time t
$m_{d,t}^{\mathrm{SL}}$	Mass flow rate of heat load d at time t
$m_{p,t}^{\mathrm{PS}}$ / $m_{p,t}^{\mathrm{PR}}$	Mass flow rate of pipeline p in the supply/return pipe at time t
$\overline{\tau}_{j,t}^{\mathrm{MS}}$ / $\underline{\tau}_{j,t}^{\mathrm{MS}}$	Max/min mixed temperature at node j of the supply pipe
$\overline{\tau}_{j,t}^{\mathrm{MR}}$ / $\underline{\tau}_{j,t}^{\mathrm{MR}}$	Max/min mixed temperature at node j of the return pipe
$N_j^{\mathrm{h}+}$ / $N_j^{\mathrm{h}-}$	Set of nodes at the start/end of DHN pipes for node j
K	Heat transfer delay coefficient
τ_t^{Am}	Predicted value of ambient temperature at period t
ξ_p	Temperature drop rate
η_p	Heat transfer coefficient of pipe p
A_p	Sectional area of pipe p
ρ_{w}	Water density
c_{w}	Specific heat capacity of water
γ_p	Time delay of mass flow in pipe p
l_p	Length of pipe p
$\overline{\tau}_p^{\mathrm{PS,out}}$	Max actual temperature of the mass flowing out of the supply pipe
$\underline{\tau}_p^{\mathrm{PS,out}}$	Min actual temperature of the mass flowing out of the supply pipe
$\overline{\tau}_p^{\mathrm{PR,out}}$	Max actual temperature of the mass flowing out of the return pipe
$\underline{\tau}_p^{\mathrm{PR,out}}$	Min actual temperature of the mass flowing out of the return pipe
C^{g}	Constant of the gas flow equation
τ^{b}	Gas temperature at the base condition
p^{b}	Gas pressure at the base condition
$D_{kk'}$	Internal diameter of the pipe from node k to k' in the NGN
$L_{kk'}$	Length of the pipeline from node k to k' in the NGN
γ^{g}	Specific gravity of natural gas
Z^{a}	Average compressibility factor
$f_{kk'}$	Friction coefficient from node k to k' in the NGN
$E_{\mathrm{g},kk'}$	Efficiency from node k to k' in the NGN
E^{Lmax}	Maximum electric load
H^{Lmax}	Maximum heat load

G^{Lmax}	Maximum gas load
α_t^{ELD}	Ratio of shiftable electric load at time t
α_t^{HLD}	Ratio of shiftable heat load at time t
α_t^{GLD}	Ratio of shiftable gas load at time t
ΔD^{EUp}	Upward climbing value of shiftable electric load
ΔD^{EDn}	Downward climbing value of shiftable electric load
ΔD^{HUp}	Upward climbing value of shiftable heat load
ΔD^{HDn}	Downward climbing value of shiftable heat load
ΔD^{GUp}	Upward climbing value of shiftable gas load
ΔD^{GDn}	Downward climbing value of shiftable gas load
$\tilde{P}_t^{\mathrm{WF}}$	Predicted output value of wind power at time t
N_{G}	Number of CON unit
p_t^{GUsr} / p_t^{GDsr}	Price of up/down SR of CON unit
N_{CHP}	Number of CHP unit
p_t^{CHPUsr} / p_t^{CHPDsr}	Price of up/down SR of CHP unit
p_t^{in} / p_t^{out}	Price of purchasing/selling electricity
r	Penalty price of wind power curtailment
p_t^{NG}	Price of purchasing NG
p_t^{XDR}	Compensate price of shiftable electric/gas/heat load
$\overline{P}_i^{\mathrm{G}}$ / $\underline{P}_i^{\mathrm{G}}$	Max/min output limits of CON unit i
$R_{i,t}^{\mathrm{GU}}$ / $R_{i,t}^{\mathrm{GD}}$	Up/down SR capacity of CON unit i
$\overline{\delta}_i^{\mathrm{G}}$ / $\underline{\delta}_i^{\mathrm{G}}$	Up/down ramp limits for CON unit i
$\overline{P}_i^{\mathrm{CHP}}$ / $\underline{P}_i^{\mathrm{CHP}}$	Max/min electric output limit of CHP unit i
$R_{i,t}^{\mathrm{CHPU}}$ / $R_{i,t}^{\mathrm{CHPD}}$	Up/down SR capacity of CHP unit i
$\overline{\delta}_i^{\mathrm{CHP}}$ / $\underline{\delta}_i^{\mathrm{CHP}}$	Up/down ramp limits for CHP unit i
Q_{ng}	High calorific value of NG
η_{CHP}	Comprehensive conversion efficiency of CHP unit
γ_{eh}	Electric heat conversion ratio of CHP unit
$\overline{P}_i^{\mathrm{PSY}}$ / $\underline{P}_i^{\mathrm{PSY}}$	Upper/lower limits of pumped power and generated power
$\hat{P}_i^{\mathrm{PSY}}$	Output change rate limit of pumping storage unit
η_i^{P2G}	P2G equipment operation efficiency
$\overline{P}_i^{\mathrm{P2G}}$ / $\underline{P}_i^{\mathrm{P2G}}$	Max/min electric power consumption for P2G
η^{EB}	Electrothermal conversion ratio of EB
$\eta_{\mathrm{in}}^{\mathrm{HS}}$ / $\eta_{\mathrm{out}}^{\mathrm{HS}}$	Heat absorption/release efficiency of HSS
$\overline{m}_j^{\mathrm{h}}$ / $\underline{m}_j^{\mathrm{h}}$	Max/min values of pipe mass flow
L^{e}	Number of power system transmission lines
$\overline{m}_l^{\mathrm{g}}$ / $\underline{m}_l^{\mathrm{g}}$	Max/min gas flow in pipeline l of the NGN
$\overline{p}_k^{\mathrm{g}}$ / $\underline{p}_k^{\mathrm{g}}$	Max/min gas pressure of NGN of node k
$\overline{P}_t^{\mathrm{in}}$ / $\underline{P}_t^{\mathrm{in}}$	Max/min value of power purchased from main grid
$\overline{P}_t^{\mathrm{out}}$ / $\underline{P}_t^{\mathrm{out}}$	Max/min value of power sold to the main grid
$\overline{G}_t^{\mathrm{in}}$ / $\underline{G}_t^{\mathrm{in}}$	Max/min value of NG purchased from the main NGN

Variables

$\tau_{p,t}^{\mathrm{PS,out}'}$ / $\tau_{p,t}^{\mathrm{PR,out}'}$	Temperature of mass flow in the supply/return pipe is measured without taking into account any temperature reduction that may occur at the outlet of the pipeline
$\tau_{p,t}^{\mathrm{PS,in}}$ / $\tau_{p,t}^{\mathrm{PR,in}}$	Temperature of the mass flow at the supply/return pipe inlet of the pipeline
$\tau_{p,t}^{\mathrm{PS,out}}$ / $\tau_{p,t}^{\mathrm{PR,out}}$	Actual temperature of the mass flowing out of the supply/return pipe at time t
$\tau_{s,t}^{\mathrm{GS}}$ / $\tau_{s,t}^{\mathrm{GR}}$	Temperature of heat source s in the supply/return pipe
$\tau_{d,t}^{\mathrm{LS}}$ / $\tau_{d,t}^{\mathrm{LR}}$	Temperature of heat load d in the supply/return pipe
$\tau_{j,t}^{\mathrm{MS}}$ / $\tau_{i,t}^{\mathrm{MR}}$	Mixed temperature at node j of the supply/return pipe
R_p	Total mass of inflow pipe p from period t- γ_p to t
$m_{kk',t}^{\mathrm{g}}$	Gas flow from node k to k' in the NGN
$\tau_{kk',t}^{\mathrm{ave}}$	Average absolute temperature of pipe from node k to k' in NGN
$m_{k,t}^{\mathrm{gs}}$	Gas supply from the gas source to node k
$m_{k,t}^{\mathrm{gd}}$	Gas consumption of node k calculated according to the gas load
E_t^{LDR}	Electric load demand considering IDR
ΔE_t^{DR}	Electric load value participating in IDR
H_t^{LDR}	Heat load demand considering IDR
ΔH_t^{DR}	Heat load value participating in IDR
G_t^{LDR}	Gas load demand considering IDR
ΔG_t^{DR}	Gas load value participating in IDR
D_ω^{PL}	Peak-valley difference of electricity-gas-heat load in the scenario ω
$X_{\omega,t}^{\mathrm{LDR}}$	Electric/gas/heat load demand considering IDR in the scenario ω
$\Delta X_{\omega,t}^{\mathrm{DR}}$	Electric/gas/heat load value participating in IDR in the scenario ω
$R_{\omega,i,t}^{\mathrm{GU}}$ / $R_{\omega,i,t}^{\mathrm{GD}}$	Up SR capacity of CON unit i in the scenario ω
$R_{\omega,i,t}^{\mathrm{CHPU}}$ / $R_{\omega,i,t}^{\mathrm{CHPD}}$	Up SR capacity of CHP unit i in the scenario ω
$P_{\omega,t}^{\mathrm{in}}$ / $P_{\omega,t}^{\mathrm{out}}$	Electricity purchased/sold in the scenario ω
$\Delta P_{\omega,t}^{\mathrm{WF}}$	Wind power curtailment in the scenario ω
$G_{\omega,t}^{\mathrm{in}}$	Amount of NG purchased from the main NGN in the scenario ω
$P_{i,t}^{\mathrm{G}}$	Electrical power output by CON unit i
$P_{i,t}^{\mathrm{CHP}}$ / $H_{i,t}$	Electrical/thermal power output by CHP unit i
$F_{i,t}^{\mathrm{CHP}}$	NG consumption of CHP unit i
$P_{i,t}^{\mathrm{PSY}}$	Output of PS unit i
$G_{i,t}^{\mathrm{P2G}}$	Gas production of P2G unit i
$P_{i,t}^{\mathrm{P2G}}$	Electric power consumed by P2G i
P_t^{EB}	Electric consumption power of EB
H_t^{EB}	Thermal power output of EB
S_t^{HS}	Heat storage capacity of HSS
H_t^{HSin} / H_t^{HSout}	Heat absorption/release power of HSS
$m_{j,t}^{\mathrm{h}}$	Pipe mass flow of the DHN

$P_{i,t}^{\mathrm{WFS}}$	Dispatching output of wind power
$P_{i,t}^{\mathrm{PSP}}$ / $P_{i,t}^{\mathrm{PSG}}$	Pumped/generated power of the PS unit i
P_t^{in} / P_t^{out}	Purchasing/selling electricity
G_t^{GSout} / G_t^{GSin}	Outflow/inflow of GS
$m_{l,t}^{\mathrm{g}}$	Gas flow of NG pipeline l

1. Introduction

With the continuous improvement of the level of electrification and the technological progress of grid connected renewable energy, diverse energy forms are now interconnected through various coupling methods. This breaks the previous situation of independent operation of traditional power, heat, natural gas (NG), and other energy systems [1]. The coordinated functioning of various energy equipment within an integrated energy system (IES) has garnered significant interest from researchers globally [2]. The coordination of renewable energy output and demand poses several risks and challenges for the integrated electric-gas-heat system (IEGHS). Specifically, there are three primary challenges:

Challenge 1: The output of large wind power resources connected to the power grid is greatly influenced by meteorological and geographical factors. To optimize dispatching efficiency, an IEGHS should consider the unpredictability of wind power generation to achieve greater cost-effectiveness.

Challenge 2: The demand response (DR) programs are highly effective in reducing power system costs [3]. However, the implementation of such programs in IEGHS with multiple interconnected energy sources presents a crucial challenge that needs to be addressed urgently.

Challenge 3: As a result of the ongoing expansion of demand-side resources and the adoption of DR initiatives, the multi-energy demand on the user side is now confronted with heightened levels of unpredictability.

Therefore, the stable economic dispatch of IEGHS needs to take into account the uncertainties on both generation and load sides, as well as the effective implementation of the integrated DR project. It is important to develop a novel optimal scheduling approach that can effectively handle multiple uncertainties in IEGHSs, as the deterministic optimal scheduling model is no longer appropriate to their scheduling requirements.

The uncertainty challenge is often addressed in existing research through the utilization of stochastic optimization (SO) and robust optimization (RO) techniques. Regarding the modeling of uncertainty, SO utilizes a probability distribution that is already known to construct the dispatch model. To tackle the stochastic dispatch problem and represent power errors in wind turbines, a flexible distribution was suggested by the authors in [4]. Additionally, [5] introduced a method for optimizing energy flow in multi-energy hub systems, accounting for uncertain variables. This model utilizes chance-constrained optimization to minimize energy costs. Meanwhile, [6] addressed the issue of how to best operate an energy hub (EH) that has multiple energy sources and is tasked with meeting unpredictable electricity and heat demands while facing uncertain prices and operational limitations.

The parameter uncertainty in RO is limited to an uncertainty set, regardless of its probability distribution. A flexible robust dispatch model was suggested by the authors in [7] to handle the uncertainty of wind power. Ref. [8] proposed a community EH model that incorporated both electrical and thermal DR programs, and employed a RO approach to address potential fluctuations in electricity prices. A robust hierarchical dispatch model was developed in [9] to tackle the

challenges of a multiphase distribution optimal power flow that incorporates uncertainties in a residential distribution network. However, obtaining the probability distribution in SO is challenging in real-world scenarios. Additionally, using RO may lead to overly cautious or risky decisions as it considers the worst-case scenario through an uncertainty set. Hence, [10] established a stochastic electricity price scenario based on the Latin hypercube sampling method, then used robust optimization methods to manage the uncertainty of renewable energy generation and load under each price scenario, and proposed a hybrid stochastic/robust optimization method to minimize the total cost of all units. A vertex scenario-based robust optimization method was studied in [11] to address the uncertainty of renewable energy in point-to-point energy trading in active distribution networks. Ref. [12] proposed a decentralized hybrid robust and stochastic expansion planning optimization method, established the Deterministic system of wind power based on robust optimization theory and the Deterministic system of load based on stochastic optimization theory, and realized the effective expansion of transmission network and active distribution network.

Integrated demand response (IDR) is also proposed to be implemented in an integrated energy system (IES) to enhance the operational efficiency of different IESs while ensuring the comfort of users [13,14]. Ref. [15] proposed a system scheduling model based on opportunity-constrained programming considering IDR in uncertain environments to minimize system operating costs and utilized IDR programming to explore the potential interaction ability between electricity-gas-heat flexible loads and electric vehicles. The IDR program is classified into an internal DR program and an external DR program. The focus in [16] is on investigating an IDR program that utilizes various energy storage devices in smart EHs. To minimize the operational cost of the IEGHS, a bi-level optimization model is developed. Similarly, [17] presented a RO dispatching model for IES. This model integrated heat-electricity DR and aimed to address the difficulties associated with operating an IES that has high levels of renewable energy penetration. Ref. [18] presented an economic dispatch model that considers environmental factors for the efficient operation of a regional energy system. The model incorporates a price-based IDR program for coordinated management.

Moreover, the variability of load demand is smaller in comparison to the unpredictability of wind energy. At present, the load uncertainty is mainly analyzed and processed by the scenario analysis technique [19]. Commonly used sampling approaches, including Monte Carlo and Latin hypercube methods, are utilized to generate multiple scenarios with probability characteristics through a probability distribution. These scenarios are then optimized to solve deterministic problems, and the optimization results from all scenarios are combined by calculating a weighted average to obtain the final optimization results [20]. However, the accuracy of the scenario-based method is highly influenced by the probability distribution function that is assumed for the load. The load characteristics are influenced by varying geographical and environmental conditions, making it challenging to utilize a standardized probability distribution function to depict them accurately. Therefore, some research results that assume one unified probability distribution function may have large errors in practice. At present, some scholars have begun to adopt generative adversarial networks (GANs) to model load uncertainty. By utilizing GANs, there is no requirement to predefine the probability distribution of data. This allows for direct learning from multi-energy load data from typical regions, ultimately leading to the creation of novel load data samples [21]. However, how to better construct the loss function of generators and discriminators in GANs to obtain ideal load scenarios needs further research.

In summary, effectively addressing uncertainties within the system and effectively implementing integrated demand

response technologies have been a major challenges and focus of the IEGHS operation. In the literature, SO and RO methods are commonly employed to handle uncertainties in renewable energy output power and load demand. While RO can address uncertain parameters with unknown probability distributions effectively, its dispatching methods often employ overly conservative but economically inefficient strategies. Therefore, when dealing with multiple uncertainties in IEGHS, it is an urgent issue to effectively utilize the advantages of SO and RO methods, which will improve the effectiveness and operational economy of IEGHS modeling. Meanwhile, although the IDR program provides a solution for the demand-side management of the IES, excessive pursuit of the economy of system operation will lead to new load peaks and valleys, undermining the performance of the IDR program.

This work presents a novel optimal scheduling approach for IEGHS that tackles the aforementioned challenges. The method integrates robust and stochastic optimization techniques and accounts for the unpredictability of both renewable energy output and multi-energy demand. Specifically, a robust stochastic optimal dispatching (RSOD) model is introduced and solved using the column and constraint generation (C&CG) method to determine the optimal scheduling plan for IEGHS in worst-case scenarios. The key contributions of this work are:

(1) A robust adjustable parameter uncertainty set is utilized in this work to define the uncertainties in output power for renewable energy. To address uncertainties related to demand side load, the paper presents a multi-energy type load scenario generation and reduction technique that employs gradient normalization improved Wasserstein generative adversarial networks (GN-WGANs) and the *K*-medoids clustering method. This method eliminates the need for probability distribution assumptions and enhances accuracy and practicality.

(2) Based on the traditional IDR model, an improved IDR (IIDR) model considering the peak-valley difference cost of the electricity-gas-heat load is proposed to effectively improve the implementation effect of DR programs and achieve better adjustment of the load curve.

(3) A two-stage RSOD model has been presented to address the uncertainty of renewable energy and load in an IEGHS, taking into account the IIDR. The model is solved using the C&CG algorithm. In the worst-case scenario, the model yields the most cost-effective scheduling plan, which is more resilient and efficient than the conventional model.

The remainder of this paper is organized as follows. Section 2 establishes the mathematical model of the integrated electric-gas-heat system. Section 3 constructs the formulation of an integrated electric-gas-heat demand response. Section 4 presents the generation and load uncertainty modeling of an IEGHS. Section 5 proposes an RSOD model for an IEGHS. Numerical tests to demonstrate the performance of our model are presented in Section 6. Conclusions are drawn in Section 7.

2. Integrated electricity-gas-heat system

IEGHSs, especially when considering the IDR and dynamic characteristics of energy networks, have been proven to be able to improve overall energy efficiency. Fig. 1 depicts the overall structural layout of IEGHS.

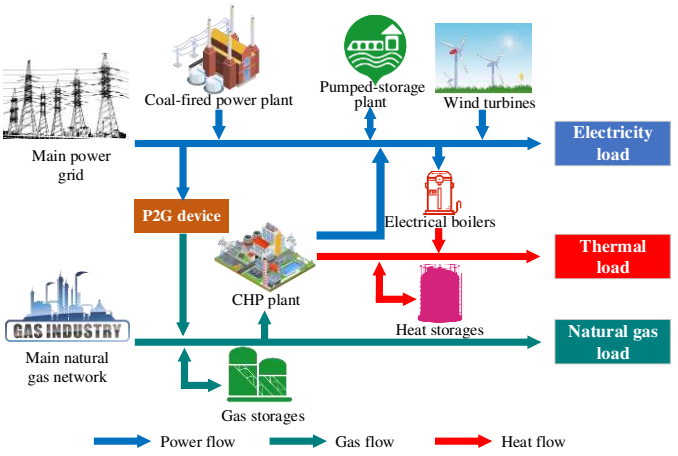

Fig.1 Overall structural layout of an IEGHS.

2.1. District heating network

A district heating network (DHN) comprises a heat source, heat load, and a water supply and return network. The system can be divided into primary and secondary networks, which are interconnected through heat exchange stations. The primary heating network (Primary DHN, PDHN) is characterized by longer pipelines containing hot water in a high-temperature, high-pressure state. It operates at a constant mass flow rate and adjusts the supply temperature to meet changes in heat demand. Thus, a constant flow-variable temperature strategy is typically employed [22]. Conversely, the secondary heating network (Secondary DHN, SDHN) uses a variable flow-constant temperature strategy. The mathematical modeling of heating networks has been thoroughly researched by various scholars; therefore, this paper will not delve into it. The general structure of nodes and pipelines of a DHN is shown in Fig. 2. *G* and *L* represent the heat source and heat load, respectively. The pipeline supplying water to the heat exchange station is depicted by the green dotted line, whereas the blue dotted line represents the pipeline transporting the returned water from the heat exchange station. For detailed modeling, please refer to [14]. The thermal inertia and heat loss models in the DHN will be detailed.

The temperatures of the nodes and the inlet/outlet points in the supply and return pipelines must adhere to temperature mixing restrictions.

$$\sum_{p\in N_j^{h-}}(\tau_{p,t}^{PS,out}m_{p,t}^{PS})=\tau_{j,t}^{MS}\sum_{p\in N_j^{h-}}m_{p,t}^{PS},\tau_{j,t}^{MS}=\tau_{p,t}^{PS,in} \tag{1}$$

$$\sum_{p\in N_j^{h+}}(\tau_{p,t}^{PR,out}m_{p,t}^{PR})=\tau_{j,t}^{MR}\sum_{p\in N_j^{h+}}m_{p,t}^{PR},\tau_{j,t}^{MR}=\tau_{p,t}^{PR,in} \tag{2}$$

$$\underline{\tau}_{j,t}^{MS}\le\tau_{j,t}^{MS}\le\overline{\tau}_{j,t}^{MS} \tag{3}$$

$$\underline{\tau}_{j,t}^{MR}\le\tau_{j,t}^{MR}\le\overline{\tau}_{j,t}^{MR} \tag{4}$$

To estimate pipeline outlet temperatures without accounting for heat loss, the nodal method suggests starting with historical inlet temperatures and considering total time delays associated with mass flow, as outlined in [23]:

$$\tau_{p,t}^{PS,out'}=K\tau_{p,t}^{PS,in}+\hat{\tau}_{p,t}^{PS,out} \tag{5}$$

$$\tau_{p,t}^{PR,out'}=K\tau_{p,t}^{PR,in}+\hat{\tau}_{p,t}^{PR,out} \tag{6}$$

In (5)-(6), $\hat{\tau}_{p,t}^{PS,out}$ and $\hat{\tau}_{p,t}^{PR,out}$ represent the influence of past inlet temperatures, which occur outside of the dispatch horizon, on the outlet temperatures of the supply and return pipes. The transfer of hot water incurs heat loss. In the

subsequent step, the outlet temperatures are adjusted to account for these heat losses.

$$\tau_{p,t}^{\mathrm{PS,out}} = \tau_t^{\mathrm{Am}} + \left(\tau_{p,t}^{\mathrm{PS,out}'} - \tau_t^{\mathrm{Am}}\right)\xi_p \tag{7}$$

$$\tau_{p,t}^{\mathrm{PR,out}} = \tau_t^{\mathrm{Am}} + \left(\tau_{p,t}^{\mathrm{PR,out}'} - \tau_t^{\mathrm{Am}}\right)\xi_p \tag{8}$$

$$\xi_p = \exp\left[-\frac{\eta_p \Delta t}{A_p \rho_{\mathrm{w}} c_{\mathrm{w}}}\left(\gamma_p + \frac{3}{2} + \frac{\rho_{\mathrm{w}} A_p l_p - R_p}{m_p^{\mathrm{PS}} \Delta t}\right)\right] \tag{9}$$

$$\underline{\tau}_p^{\mathrm{PS,out}} \le \tau_{p,t}^{\mathrm{PS,out}} \le \overline{\tau}_p^{\mathrm{PS,out}} \tag{10}$$

$$\underline{\tau}_p^{\mathrm{PR,out}} \le \tau_{p,t}^{\mathrm{PR,out}} \le \overline{\tau}_p^{\mathrm{PR,out}} \tag{11}$$

2.2. Natural gas network

The NGN system comprises gas wells, pipelines, compressors, and users. In this work, it is assumed that the gas flow characteristics remain constant throughout each dispatching period. Furthermore, the steady-state mathematical model is utilized to take into account the limitations of the NG system. NG has different characteristics from electric power which features simultaneous generation, transmission, and consumption. The natural gas (NG) transmission speed is relatively slow and can be compressed, which can cause variations in flow and pressure between the inlet and outlet of gas pipelines [24]. Fig. 3 provides a general overview of the nodes and pipelines that comprise an NGN.

The flow and node balance of NG pipelines is represented by the following equations [25]:

$$m_{kk',t}^{\mathrm{g}} = C^{\mathrm{g}}\left(\frac{\tau^{\mathrm{b}}}{p^{\mathrm{b}}}\right) D_{kk'}^{2.5} E_{\mathrm{g},kk'} \sqrt{\left(\frac{(p_{k,t}^{\mathrm{g}})^2 - (p_{k',t}^{\mathrm{g}})^2}{L_{kk'} \cdot \gamma^{\mathrm{g}} \cdot \tau_{kk',t}^{\mathrm{ave}} \cdot Z^{\mathrm{a}} \cdot f_{kk'}}\right)}, \forall t \in T \wedge \forall k,k' \in N_{\mathrm{g}} \tag{12}$$

$$(\Delta p_{kk',t}^{\mathrm{g}})^2 = (p_{k,t}^{\mathrm{g}})^2 - (p_{k',t}^{\mathrm{g}})^2 - Z_{kk'}(m_{kk',t}^{\mathrm{g}})^2, \forall t \in T \wedge \forall k,k' \in N_{\mathrm{g}} \tag{13}$$

$$\Delta m_{k,t}^{\mathrm{g}} = m_{k,t}^{\mathrm{gs}} - m_{k,t}^{\mathrm{gd}} - \sum_{k' \in N_{\mathrm{g}}} m_{kk',t}^{\mathrm{g}} \quad , \forall t \in T \wedge \forall k,k' \in N_{\mathrm{g}} \tag{14}$$

In (13), $Z_{kk'}$ is the pipeline resistance from node k to node k' in the NGN. Equations (13)-(14) represent the flow and node balance of the NG pipeline, respectively.

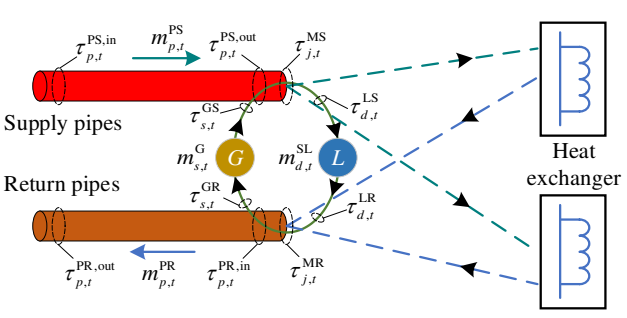

Fig. 2 A general structure of the nodes and pipelines of a DHN.

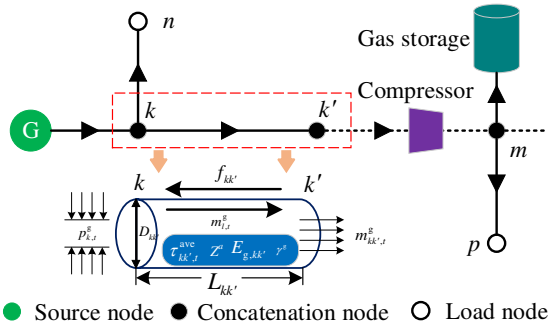

Fig. 3 A general structure of nodes and pipelines of an NGN.

3. The formulation of integrated electricity-gas-heat demand response

3.1. Electricity demand response model

This paper focuses on the load-based incentive DR approach for managing electric load demand.

$$E_t^{\mathrm{LDR}} = \Delta E_t^{\mathrm{DR}} + E_t^{\mathrm{L}} \tag{15}$$

In (15), E_t^{L} is the magnitude of electric/gas/heat load without considering DR.

The constraint for adjusting the electric load is expressed as:

$$E_t^{\mathrm{L}} - E^{\mathrm{Lmax}} \le \Delta E_t^{\mathrm{DR}} \le \alpha_t^{\mathrm{ELD}} E_t^{\mathrm{L}} \tag{16}$$

$$E_t^{\mathrm{LDR}} - E_{t-1}^{\mathrm{LDR}} \le \Delta D^{\mathrm{EUp}} \tag{17}$$

$$E_{t-1}^{\mathrm{LDR}} - E_t^{\mathrm{LDR}} \le \Delta D^{\mathrm{EDn}} \tag{18}$$

3.2. Heat demand response model

This paper does not take into account the interruption cost in the heat capacity difference due to the thermal inertia of DHN. The relationship between predicted load, planned load, and heat DR is demonstrated in Equation (19), while the heat demand response limit is illustrated in (20). In addition, constraints on the power limit of heat load ramping under a continuous time scale are constructed as shown in equations (21)-(22).

$$H_t^{\mathrm{LDR}} = \Delta H_t^{\mathrm{DR}} + H_t^{\mathrm{L}} \tag{19}$$

$$H_t^{\mathrm{L}} - H^{\mathrm{Lmax}} \le \Delta H_t^{\mathrm{DR}} \le \alpha_t^{\mathrm{HLD}} H_t^{\mathrm{L}} \tag{20}$$

$$H_t^{\mathrm{LDR}} - H_{t-1}^{\mathrm{LDR}} \le \Delta D^{\mathrm{HUp}} \tag{21}$$

$$H_{t-1}^{\mathrm{LDR}} - H_t^{\mathrm{LDR}} \le \Delta D^{\mathrm{HDn}} \tag{22}$$

For the heat DR, due to people are not sensitive to small temperature changes, the temperature can be controlled within a comfortable range, to further improve the economy of the IEGHS. The predicted mean vote (PMV) [26] and thermal sensation vote [14] methods are usually used to characterize the thermal comfort of users. The PMV index is classified into seven grades, each corresponding to one of the seven senses of the human body, so it can well describe people's perception of temperature changes. A PMV value of 0 indicates the optimal thermal comfort level for indoor environments. PMV values of "+1", "+2", and "+3" represent slightly warm, warm, and hot conditions, while PMV values of "-1", "-2", and "-3" indicate slightly cool, cool, and cold temperatures.

$$PMV_t = (0.303 \times \exp\{-0.05 \times M_t\} + 0.028) \times H_t^{\mathrm{L}} \tag{23}$$

In (23), M_t denotes human body heat/power production. The change of heat load at time t is obtained by calculating the value of PMV in the interval (-1, 1).

Determine the final heat load demand value based on τ_t^{in} and [$\tau_0^{\mathrm{in,low}}$, $\tau_0^{\mathrm{in,high}}$].

$$\Delta H_t^{\mathrm{DR}} = f\left(\tau_t^{\mathrm{in}}\right) - f\left(\tau_t^{\mathrm{in}} - \Delta\tau_t^{\mathrm{in}}\right) \tag{24}$$

$$\tau_t^{\mathrm{in,low}} \le \tau_t^{\mathrm{in}} - \Delta\tau_t^{\mathrm{in}} \le \tau_t^{\mathrm{in,high}} \tag{25}$$

In (24)-(25), $f\left(\tau_t^{\mathrm{in}}\right)$ is the function of heat load and indoor temperature. τ_t^{in} is the indoor temperature at time t. $\Delta\tau_t^{\mathrm{in}}$ is the acceptable indoor temperature deviation. $\tau_t^{\mathrm{in,high}}$ and $\tau_t^{\mathrm{in,low}}$ are the max and min acceptable indoor temperatures, respectively.

3.3. Gas demand response model

To develop a demand response (DR) model for the gas grid, this paper investigates the electricity load DR mechanism and focused on a gas load DR model based on price. The maximum adjustable load for each time interval of the gas load demand is represented by Equation (26), while Equation (27) shows the natural gas load demand after the implementation of IDR. Additionally, the load ramp rate in continuous time is modeled with Equations (28)-(29).

$$G_t^{\mathrm{L}} - G^{\mathrm{Lmax}} \le \Delta G_t^{\mathrm{DR}} \le \alpha_t^{\mathrm{GLD}} G_t^{\mathrm{L}} \tag{26}$$

$$G_t^{\mathrm{LDR}} = \Delta G_t^{\mathrm{DR}} + G_t^{\mathrm{L}} \tag{27}$$

$$G_t^{\mathrm{LDR}} - G_{t-1}^{\mathrm{LDR}} \le \Delta D^{\mathrm{GUp}} \tag{28}$$

$$G_{t-1}^{\mathrm{LDR}} - G_t^{\mathrm{LDR}} - \le \Delta D^{\mathrm{GDn}} \tag{29}$$

4. Generation and load uncertainty modeling of an IEGHS

Due to the integration of different types of energy equipment, IEGHS is characterized by significant uncertainty and modeling complexity. This section analyzes and establishes appropriate mathematical models for uncertainties in wind output power and load demand.

4.1. Robust uncertainty set

The output of WTs is heavily influenced by meteorological conditions and the geographical environment, with strong uncertainty and intermittency. Moreover, its prediction error is relatively large [27], and it is difficult to accurately grasp the operation rules of WTs. The uncertainty of wind power is a haphazard uncertainty that can be repeated in high frequencies and short periods, and due to insufficient data, it is difficult to accurately fit into any distribution. Hence, robust optimization methods are adopted to address the uncertainty of wind power.

The robust optimization method only requires a set of uncertainties rather than a probability distribution function to represent haphazard uncertainties and make scheduling decisions in the worst-case scenario of these sets. The selection of uncertain sets is the key to handling uncertain robust optimization problems, and it is necessary to select uncertain sets that do not increase the computational difficulty of the model based on the characteristics of uncertain parameters. At present, uncertain sets are usually described using boxes and ellipsoids. However, the commonly used uncertainty set expression has a large margin of uncertainty, which leads to overly conservative scheduling results and affects the economy of scheduling results. To describe the fluctuation of uncertainty and obtain scheduling schemes under different risks, this paper adopts a robust uncertainty set with adjustable parameters to describe the uncertainty of wind power. By utilizing an uncertainty set with robust adjustable parameters, it is possible to effectively control the impact of uncertainty shifts and more accurately measure uncertainty fluctuations. The uncertainty set can be formulated as follows:

$$\mathcal{U} = \{\tilde{P}_t^{\mathrm{WF}} \left| \tilde{P}_t^{\mathrm{WF}} = \hat{P}_t^{\mathrm{WF}} + u_t^{\mathrm{W}+}\Delta P_t^{\mathrm{WF}} - u_t^{\mathrm{W}-}\Delta P_t^{\mathrm{WF}}, u_t^{\mathrm{W}+} + u_t^{\mathrm{W}-} \le 1, \sum_{t\in T}(u_t^{\mathrm{W}+} + u_t^{\mathrm{W}-}) \le \Gamma^{\mathrm{W}}, \Gamma^{\mathrm{W}} \in [0,T],\} \right. \tag{30}$$

In (30), $\tilde{P}_t^{\mathrm{WF}}$ is the output of wind power at t. $\Delta P_t^{\mathrm{WF}} = (\bar{P}_t^{\mathrm{WF}} - \underline{P}_t^{\mathrm{WF}})/2$ is the fluctuation range of forecasted values. $u_t^{\mathrm{W}+}$ and $u_t^{\mathrm{W}-}$ are binary variables. Γ^{W} is a budget parameter with a value range of [0, T], indicating the number of periods in which the wind power reaches the boundary value of the fluctuation range during the scheduling period. The conservatism of the model can be adjusted by adjusting Γ^{W}, and the larger the numerical value, the more conservative the preference for scheduling scheme risks.

4.2. Uncertainty modeling of load demand

In this work, an improved Wasserstein GANs based on gradient normalization (GN-WGANs) is proposed to generate a set of electric/thermal/gas load demand scenarios, and then apply the *K*-medoids algorithm to obtain typical scenarios. By incorporating Wasserstein distance into the GANs model, the distance between two different distributions can be calculated directly, which is consistent with the confrontation game theory between two neural networks in the GANs model. The expression is as follows:

$$W(D(s_r), D(G(z))) = \sup_{\theta^D} \left\{ E_{Sr}\left[D(s_r)\right] - E_z\left[D(G(z))\right] \right\} \tag{31}$$

$$L_{\mathrm{D}} = -E_{Sr}\left[log\left(D(s_r;\theta^{\mathrm{D}})\right)\right] - E_z\left[log\left(1-D(s_g;\theta^{\mathrm{D}})\right)\right] \tag{32}$$

$$L_{\mathrm{G}} = -E_z\left[log\left(1-D(G(z;\theta^{\mathrm{G}});\theta^{\mathrm{D}})\right)\right] \tag{33}$$

In (31)-(33), $D(\cdot)$ represents the discriminator. $G(\cdot)$ represents the generator. z represents random noise. s_r represents the real samples. sup$(\cdot)$ represents the supremum function. E_{Sr} and E_z represent the expected value of all real samples and the expected value of all random input samples of the generator, respectively. L_{D} and L_{G} represent the loss function of the discriminator and generator. s_g represents the generated samples. θ^{D} and θ^{G} represent the network parameters of the discriminator and generator, respectively.

Despite the ability of WGANs to generate desired scenarios with improved performance for modeling real distributions, it remains a significant challenge to ensure that the Lipschitz constraint is met in GANs models while also achieving a good balance between the constraint and network capacity. The weight clipping and regularization in [28] are applied to allow the networks to search in large function space but loosen the Lipschitz constraint. As shown in reference [29], the Lipschitz constant of a layer-wise 1-Lipschitz constraint may decrease significantly as the number of layers increases. The related proof can be seen in [29]. It should be emphasized that the potential reduction in the Lipschitz constant as the number of layers increases is a key factor contributing to the incompatibility between spectral normalization GANs [30] and Wasserstein distance when gradient-based regularization is not utilized. To clarify, a network that is constrained by a model-wise Lipschitz constraint may not require a layer-wise Lipschitz constraint, and it may be necessary to construct a network with such a constraint. Driven by the issues, the gradient normalization (GN) method is designed to address the above-mentioned problem, which could achieve a better compromise between the gradient norm limitation and discriminator capacity. The GN-based method normalizes both the gradient and the boundary norm:

$$\hat{L}_D(s) = \frac{L_D(s)}{\left\|\nabla_s L_D(s)\right\| + \xi(s)} \tag{34}$$

In (34), $\hat{L}_{\mathrm{D}}(s)$ denotes the GN form of L_{D}. $\left\|\nabla_s L_{\mathrm{D}}(s)\right\|$ denotes the gradient of L_{D}. $\xi(s)$ is a universal term that can be set as a function associated with $L_{\mathrm{D}}(s)$ or a constant value. Here, this paper sets the $\xi(s)$ to be $L_{\mathrm{D}}(s)$[29]. The (34) can be rewritten as:

$$\hat{L}_D(s) = \frac{L_D(s)}{\left\|\nabla_s L_D(s)\right\| + L_D(s)} \tag{35}$$

Under this setting, the normalized gradient norm $\left\|\nabla_s \hat{L}_{\mathrm{D}}(s)\right\|$ is close to 0 when the discriminator is saturated due to overfitting (the related proof can be seen in [29]).

This article further derives the gradient of $\hat{L}_{\mathrm{D}}(s)$ to the parameters $\boldsymbol{W}_k$ of the k^{th} layer.

$$\begin{aligned}\frac{\partial \hat{L}_D}{\partial \mathbf{W}_k} &= \frac{\partial \hat{L}_D}{\partial L_D}\frac{\partial L_D}{\partial \mathbf{W}_k} + \frac{\partial \hat{L}_D}{\partial \left\|\nabla_s L_D\right\|}\frac{\partial \left\|\nabla_s L_D\right\|}{\partial \mathbf{W}_k} = \frac{\left\|\nabla_s L_D\right\|}{(\left\|\nabla_s L_D\right\| + \left|L_D\right|)^2}\frac{\partial L_D}{\partial \mathbf{W}_k} - \frac{L_D}{(\left\|\nabla_s L_D\right\| + \left|L_D\right|)^2}\frac{\partial \left\|\nabla_s L_D\right\|}{\partial \mathbf{W}_k} \\ &= \frac{1}{(\left\|\nabla_s L_D\right\| + \left|L_D\right|)^2}\left(\left\|\nabla_s L_D\right\|\frac{\partial L_D}{\partial \mathbf{W}_k} - f\frac{\partial \left\|\nabla_s L_D\right\|}{\partial \mathbf{W}_k}\right)\end{aligned} \tag{36}$$

Through deriving the gradient of $\hat{L}_{\mathrm{D}}(s)$ to the $\boldsymbol{W}_k$, it can be seen that in the first line of (36), the first term of which refers to the gradient of the GANs objective, which enhances the discrimination performance. Simultaneously, the second term in the equation represents a form of regularization that penalizes the gradient norm of the discriminator, with an adaptive regularization coefficient. From the last line of (36), it can be seen that the GN is a special form of an adaptive GN. Compared with zero-centered gradient penalty (0-GP) [31] and 1-centered gradient penalty (1-GP) [32], the GN is more flexible and could be adjusted automatically according to the GAN loss.

Trained GN-WGANs can be utilized to generate various load scenarios. Specifically, they can generate N power, heat, and gas load scenarios, resulting in a total of N^3 possible combinations. With an increase in N, the model's computational burden and complexity significantly rise due to the sharp growth of combined scenarios. Therefore, it is necessary to reduce scenes to improve computational efficiency. However, too few scenarios can also have a negative impact on the accuracy of scheduling results. To address this issue, clustering methods are often employed to reduce the number of scenarios. Compared to the conventional K-means method, the K-medoids method employs a central sample point as the clustering center, which minimizes the direct impact of outlier data on the clustering results and leads to superior clustering performance. The K-medoids approach is employed to decrease the number of situations for various load categories. This is accomplished by selecting scenarios with unique characteristics and a high likelihood from the initial dataset [33]. The calculation steps of the K-medoids method are detailed in [34]. The index of Davies-Bouldin (IDB) [35] was used to determine the appropriate number of cluster centers. By setting the number of cluster centers in the K-medoids method, an optimized cluster centers can be obtained through the clustering process. After reducing the typical scenario of electricity-gas-heat load demand, the probability of each type of scenario can be calculated by $\pi_k=N_k / N$.

After the reduction, the numbers of electric, heat, and gas load demand scenarios of the system are S_{e}, S_{h}, and S_{g}, respectively. The number of electricity-heat-gas load typical scenarios generated for IEGHS is $S=S_{\mathrm{e}}S_{\mathrm{h}}S_{\mathrm{g}}$. The probability of electric, heat, and gas load scenarios is π_{e}, π_{h}, and π_{g}, respectively. The probability value in any scenario is $\pi_\omega = \pi_{\mathrm{e}}\pi_{\mathrm{h}}\pi_{\mathrm{g}}$. The set of electricity-gas-heat load demand scenarios is defined as $\mathcal{G}=[1,\ 2,\ \ldots\omega,\ldots S]$.

5. Robust stochastic optimal dispatching model for IEGHS

The RSOD problem for an IEGHS is investigated based on established mathematical models of wind output power and load demand, which are inherently uncertain.

5.1. Objective function

The mathematical expression of the two-stage RSOD model is as follows,

$$\min\left[\sum_{\omega\in C}\pi_\omega\left(\lambda D_\omega^{\mathrm{PL}}+C_\omega^{\mathrm{SR}}\right)+\max_{u\in\mathcal{U}}\min\sum_{t\in T}\left(C_{\omega,t}^{\mathrm{Pur}}+C_{\omega,t}^{\mathrm{WF}}+C_{\omega,t}^{\mathrm{PNG}}+C_{\omega,t}^{\mathrm{XDR}}\right)\right] \tag{37}$$

$$D_\omega^{\mathrm{PL}}=\left(\max_{t\in T}X_{\omega,t}^{\mathrm{LDR}}-\min_{t\in T}X_{\omega,t}^{\mathrm{LDR}}\right),X\in\{P,H,G\} \tag{38}$$

$$C_\omega^{\mathrm{SR}}=\sum_{t\in T}\left[\sum_{i=1}^{N_{\mathrm{G}}}\left(p_t^{\mathrm{GUsr}}R_{\omega,i,t}^{\mathrm{GU}}+p_t^{\mathrm{GDsr}}R_{\omega,i,t}^{\mathrm{GD}}\right)+\sum_{i=1}^{N_{\mathrm{CHP}}}\left(p_t^{\mathrm{CHPUsr}}R_{\omega,i,t}^{\mathrm{CHPU}}+p_t^{\mathrm{CHPDsr}}R_{\omega,i,t}^{\mathrm{CHPD}}\right)\right] \tag{39}$$

$$C_{\omega,t}^{\mathrm{Pur}}=p_t^{\mathrm{in}}P_{\omega,t}^{\mathrm{in}}-p_t^{\mathrm{out}}P_{\omega,t}^{\mathrm{out}} \tag{40}$$

$$C_{\omega,t}^{\mathrm{WF}}=r\Delta P_{\omega,t}^{\mathrm{WF}} \tag{41}$$

$$C_{\omega,t}^{\mathrm{PNG}} = p_t^{\mathrm{NG}} G_{\omega,t}^{\mathrm{in}} \tag{42}$$

$$C_{\omega,t}^{\mathrm{XDR}} = p_t^{\mathrm{XDR}} \left|\Delta X_{\omega,t}^{\mathrm{DR}}\right|, X \in \{E,H,G\} \tag{43}$$

In (37), π_ω is the probability in the scenario ω. λ is the cost coefficient of peak-valley difference. C_ω^{SR} is the cost of spinning reserve (SR). $\mathcal{U}$ represents uncertainty set. $C_{\omega,t}^{\mathrm{Pur}}$ is the cost of purchasing/selling electricity. $C_{\omega,t}^{\mathrm{WF}}$ is the penalty cost for wind power curtailment. $C_{\omega,t}^{\mathrm{PNG}}$ is the cost of purchase NG. $C_{\omega,t}^{\mathrm{XDR}}$ is the compensation for shiftable electric/gas/heat load. Equation (37) represents the objective function of the two-stage RSOD model. Equation (38) represents the peak-to-valley difference of the electric-thermal load. Equation (39) represents the spinning reserve cost of the units. Equation (40) represents the cost of purchasing and selling electricity. Equation (41) represents the cost of the wind curtailment penalty. Equation (42) represents the cost of purchasing gas. Equation (43) represents the integrated DR compensation cost for the electric-gas-heat load.

5.2. Constraints

To solve the RSOD model, the following constraints must also be met (to simplify the description, all constraints are operational constraints in the scenario ω):

1) Operation constraints of CON units:

$$\underline{P}_i^{\mathrm{G}} \le P_{i,t}^{\mathrm{G}} \le \overline{P}_i^{\mathrm{G}} \tag{44}$$

$$\begin{cases} P_{i,t-1}^{\mathrm{CON}} - P_{i,t}^{\mathrm{CON}} - R_{i,t}^{\mathrm{GD}} \le \underline{\delta}_i^{\mathrm{G}} \Delta t,\ R_{i,t}^{\mathrm{GD}} \le \underline{\delta}_i^{\mathrm{G}} \\ P_{i,t}^{\mathrm{CON}} - P_{i,t-1}^{\mathrm{CON}} + R_{i,t}^{\mathrm{GU}} \le \overline{\delta}_i^{\mathrm{G}} \Delta t,\ R_{i,t}^{\mathrm{GU}} \le \overline{\delta}_i^{\mathrm{G}} \end{cases} \tag{45}$$

2) Operation constraints of CHP units:

$$\underline{P}_i^{\mathrm{CHP}} \le P_{i,t}^{\mathrm{CHP}} \le \overline{P}_i^{\mathrm{CHP}} \tag{46}$$

$$\begin{cases} P_{i,t-1}^{\mathrm{CHP}} - P_{i,t}^{\mathrm{CHP}} - R_{i,t}^{\mathrm{CHPD}} \le \underline{\delta}_i^{\mathrm{CHP}} \Delta t,\ R_{i,t}^{\mathrm{CHPD}} \le \underline{\delta}_i^{\mathrm{CHP}} \\ P_{i,t}^{\mathrm{CHP}} - P_{i,t-1}^{\mathrm{CHP}} + R_{i,t}^{\mathrm{CHPU}} \le \overline{\delta}_i^{\mathrm{CHP}} \Delta t,\ R_{i,t}^{\mathrm{CHPU}} \le \overline{\delta}_i^{\mathrm{CHP}} \end{cases} \tag{47}$$

$$P_{i,t}^{\mathrm{CHP}} = \eta_{\mathrm{CHP}} Q_{\mathrm{ng}} F_{i,t}^{\mathrm{CHP}} \tag{48}$$

$$H_{i,t} = \gamma_{\mathrm{eh}} P_{i,t}^{\mathrm{CHP}} \tag{49}$$

3) Operation constraints of PS units:

$$\underline{P}_i^{\mathrm{PSY}} \le P_{i,t}^{\mathrm{PSY}} \le \overline{P}_i^{\mathrm{PSY}}, \mathrm{Y} \in \{\mathrm{P},\mathrm{G}\} \tag{50}$$

$$\left|P_{i,t}^{\mathrm{PSY}} - P_{i,t-1}^{\mathrm{PSY}}\right| \le \hat{P}_i^{\mathrm{PSY}}, \mathrm{Y} \in \{\mathrm{P},\mathrm{G}\} \tag{51}$$

$$P_{i,t}^{\mathrm{PSG}} P_{i,t}^{\mathrm{PSP}} = 0 \tag{52}$$

4) Operation constraints of P2G equipment：

$$G_{i,t}^{\mathrm{P2G}} = \eta_i^{\mathrm{P2G}} P_{i,t}^{\mathrm{P2G}} / Q_{\mathrm{ng}} \tag{53}$$

$$\underline{P}_i^{\mathrm{P2G}} \le P_{i,t}^{\mathrm{P2G}} \le \overline{P}_i^{\mathrm{P2G}} \tag{54}$$

5) Operation constraints of EB:

$$H_t^{\mathrm{EB}} = \eta^{\mathrm{EB}} P_t^{\mathrm{EB}} \tag{55}$$

$$H_t^{\mathrm{EB}} = H_t^{\mathrm{EBD}} + H_t^{\mathrm{HSin}} \tag{56}$$

6) Operation constraints of HSS:

$$S_t^{\mathrm{HS}} = S_{t-1}^{\mathrm{HS}} + \left(\eta_{\mathrm{in}}^{\mathrm{HS}} H_t^{\mathrm{HSin}} - \eta_{\mathrm{out}}^{\mathrm{HS}} H_t^{\mathrm{HSout}}\right) \Delta T \tag{57}$$

$$0 \le H_t^{\mathrm{HSin}} \le \eta_{\mathrm{in}}^{\mathrm{HS}} S^{\mathrm{HS}} \tag{58}$$

$$0 \le H_t^{\mathrm{HSout}} \le \eta_{\mathrm{out}}^{\mathrm{HS}} S^{\mathrm{HS}} \tag{59}$$

$$H_t^{\mathrm{HSin}} H_t^{\mathrm{HSout}} = 0 \tag{60}$$

7) Pipeline constraints of DHN:

In addition to satisfying the constraints of equations (1)-(11), the mass flow of pipelines in DHN must also meet the following constraint.

$$\underline{m}_j^{\mathrm{h}} \le m_{j,t}^{\mathrm{h}} \le \overline{m}_j^{\mathrm{h}} \tag{61}$$

8) Electric/thermal power balance constraint:

$$\sum_{i=1}^{N_{\mathrm{G}}} P_{i,t}^{\mathrm{G}} + \sum_{i=1}^{N_{\mathrm{CHP}}} P_{i,t}^{\mathrm{CHP}} + \sum_{i=1}^{N_{\mathrm{W}}} P_{i,t}^{\mathrm{WFS}} + \sum_{i=1}^{N_{\mathrm{PS}}} P_{i,t}^{\mathrm{PSG}} + P_t^{\mathrm{in}} = E_t^{\mathrm{LDR}} + \sum_{i=1}^{N_{\mathrm{P}}} P_{i,t}^{\mathrm{P2G}} + \sum_{n=1}^{N_{\mathrm{E}}} P_{i,t}^{\mathrm{EB}} + \sum_{i=1}^{N_{\mathrm{PS}}} P_{i,t}^{\mathrm{PSP}} + P_t^{\mathrm{out}} \tag{62}$$

$$\sum_{j=1}^{N_{\mathrm{CHP}}} H_{i,t} + H_t^{\mathrm{EB}} + H_t^{\mathrm{HSout}} = H_t^{\mathrm{LDR}} \tag{63}$$

9) Gas demand balance constraint considering NGN storage characteristics:

$$G_t^{\mathrm{in}} + \sum_i G_{i,t}^{\mathrm{P2G}} + G_t^{\mathrm{GSout}} - G_t^{\mathrm{GSin}} = \sum_i F_{i,t}^{\mathrm{CHP}} + G_t^{\mathrm{LDR}} + \sum_{l \in \Phi_{\mathrm{p}}^{\mathrm{Gas}}} m_{l,t}^{\mathrm{g}} \tag{64}$$

In (64), $\Phi_{\mathrm{p}}^{\mathrm{Gas}}$ is the set of NG pipelines.

10) Gas flow constraints are,

$$\underline{m}_l^{\mathrm{g}} \le m_{l,t}^{\mathrm{g}} \le \overline{m}_l^{\mathrm{g}}, \forall t \in T \wedge l \in \Phi_{\mathrm{p}}^{\mathrm{Gas}} \tag{65}$$

$$\underline{p}_k^{\mathrm{g}} \le p_{k,t}^{\mathrm{g}} \le \overline{p}_k^{\mathrm{g}} \quad , \forall t \in T \wedge \forall k \in N_{\mathrm{g}} \tag{66}$$

11) Other constraints:

Other basic operation constraints include power exchange constraints with the main grid, NG procurement constraints of the main NGN, and electric/gas/heat load constraints after participating in IDR.

$$\underline{P}_t^{\mathrm{in}} \le P_t^{\mathrm{in}} \le \overline{P}_t^{\mathrm{in}} \tag{67}$$

$$\underline{P}_t^{\mathrm{out}} \le P_t^{\mathrm{out}} \le \overline{P}_t^{\mathrm{out}} \tag{68}$$

$$\underline{G}_t^{\mathrm{in}} \le G_t^{\mathrm{in}} \le \overline{G}_t^{\mathrm{in}} \tag{69}$$

$$\begin{cases} \max\limits_{t \in T} X_{\omega,t}^{\mathrm{L}} \ge X_{\omega}^{\mathrm{Lave}} \\ \min\limits_{t \in T} X_{\omega,t}^{\mathrm{L}} \le X_{\omega}^{\mathrm{Lave}} \end{cases}, X \in \{E, H, G\} \tag{70}$$

In (70), $X_{\omega}^{\mathrm{Lave}}$ is the average value of electric/heat/gas load.

The DC power flow method is adopted in this work for calculation [36]. The operation constraints of GSS and the transaction constraints of electricity and NG can be found in [17].

5.3. Solution algorithm

The RSOD model presented in this paper involves both maximizing and minimizing problems, which poses a significant challenge for direct model solving. The decomposition algorithms can be used to solve this problem. Benders decomposition method [37] and the C&CG method [14] are often used in literature, both of which can obtain accurate solutions. The C&CG method is similar to the Benders decomposition method in that it iteratively generates cutting surfaces. The difference is that the Benders decomposition method relies on the dual representation of the Linear programming subproblem to generate the dual cut, while the C&CG method introduces the original cut with new variables by solving the two-level subproblem [14]. It was tested and pointed out in the Refs [38,39] that the Benders decomposition method requires more iterations to converge. Therefore, this paper adopts the C&CG method to solve the established RSOD model. The compact expression for the RSOD model is:

$$\begin{cases} \min\limits_{\substack{\boldsymbol{x}\\ \omega\in\mathcal{G}}} \left\{ \boldsymbol{a}^{\mathrm{T}}\boldsymbol{x} + \max\limits_{u\in\mathcal{U}} \min\limits_{\boldsymbol{y}\in\boldsymbol{M}(\boldsymbol{y},u)} \boldsymbol{b}^{\mathrm{T}}\boldsymbol{y} \right\} \\ s.t.\ \boldsymbol{C}\boldsymbol{x} \le \boldsymbol{h} \\ \quad \boldsymbol{Q}(\boldsymbol{y},u) = \left\{ \boldsymbol{D}\boldsymbol{x} + \boldsymbol{E}\boldsymbol{y} + \boldsymbol{F}\boldsymbol{u} \le \boldsymbol{g} \right\} \end{cases} \tag{71}$$

Based on the principle of the C&CG method, the primal problem is divided into the MP and SP to be solved separately. The MP and SP with the RSOD model are:

$$\mathrm{MP}: \begin{cases} \min\limits_{\boldsymbol{x},\boldsymbol{y},\eta} \boldsymbol{a}^{\mathrm{T}}\boldsymbol{x} + \eta \\ s.t. \boldsymbol{C}\boldsymbol{x} \le \boldsymbol{h} \\ \quad \eta \ge \boldsymbol{b}^{\mathrm{T}}\boldsymbol{y}^{l} \\ \quad \boldsymbol{D}\boldsymbol{x} + \boldsymbol{E}\boldsymbol{y}^{l} + \boldsymbol{F}\boldsymbol{u}_{*}^{l} \le \boldsymbol{g} \end{cases} \tag{72}$$

$$\mathrm{SP}: \begin{cases} \psi(\boldsymbol{x}) = \max\limits_{u\in\mathcal{U}} \min\limits_{\boldsymbol{y}\in\boldsymbol{M}(\boldsymbol{y},u)} \boldsymbol{b}^{\mathrm{T}}\boldsymbol{y} = \max\limits_{u\in\mathcal{U},\boldsymbol{\mu}} \boldsymbol{\mu}^{\mathrm{T}}(\boldsymbol{g} - \boldsymbol{D}\boldsymbol{x} - \boldsymbol{F}\boldsymbol{u}) \\ s.t.\ \boldsymbol{\mu}^{\mathrm{T}}\boldsymbol{E} = \boldsymbol{b}^{\mathrm{T}}, \boldsymbol{\mu} \ge 0 \end{cases} \tag{73}$$

In (73), $\boldsymbol{\mu}$ is a dual variable corresponding to the constraint. When solving the RSOD model, there are non-linear terms involving two real variables whose product is 0, such as $P_{i,t}^{\mathrm{PSG}} P_{i,t}^{\mathrm{PSP}} = 0$, $H_t^{\mathrm{HSin}} H_t^{\mathrm{HSout}} = 0$. These nonlinear terms can be linearized by introducing binary variables and adding the following constraints.

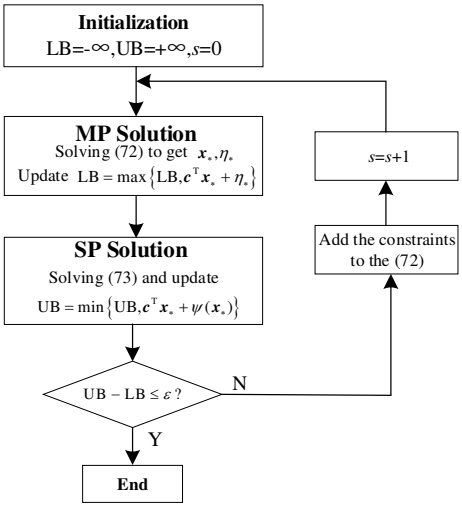

Fig. 4. Solution flow chart based on C&CG.

$$\begin{cases} 0 \le H_t^{\mathrm{HSin}} \le \xi_t^{\mathrm{HS}} \eta_{\mathrm{in}}^{\mathrm{HS}} S^{\mathrm{HS}} \\ 0 \le H_t^{\mathrm{HSout}} \le \zeta_t^{\mathrm{HS}} \eta_{\mathrm{out}}^{\mathrm{HS}} S^{\mathrm{HS}} \\ 0 \le \xi_t^{\mathrm{HS}} + \zeta_t^{\mathrm{HS}} \le 1 \end{cases} \tag{74}$$

$$\begin{cases} \xi_{i,t}^{\mathrm{PS}} \underline{P}_i^{\mathrm{PSG}} \le P_{i,t}^{\mathrm{PSG}} \le \xi_{i,t}^{\mathrm{PS}} \overline{P}_i^{\mathrm{PSG}} \\ \zeta_{i,t}^{\mathrm{PS}} \underline{P}_i^{\mathrm{PSP}} \le P_{i,t}^{\mathrm{PSP}} \le \zeta_{i,t}^{\mathrm{PS}} \overline{P}_i^{\mathrm{PSP}} \\ 0 \le \xi_{i,t}^{\mathrm{PS}} + \zeta_{i,t}^{\mathrm{PS}} \le 1 \end{cases} \tag{75}$$

The solution process based on C&CG is shown in Fig. 4.

6. Case study

To evaluate the proposed RSOD model, an example IEGHS consisting of a modified 9-bus electric power network, a 6-bus NGN, and a modified 6-bus DHN is shown in Fig. 5. The simulation parameters for a 6-bus NGN are derived from [40] The simulation data of a 6-bus DHN is given in [41].

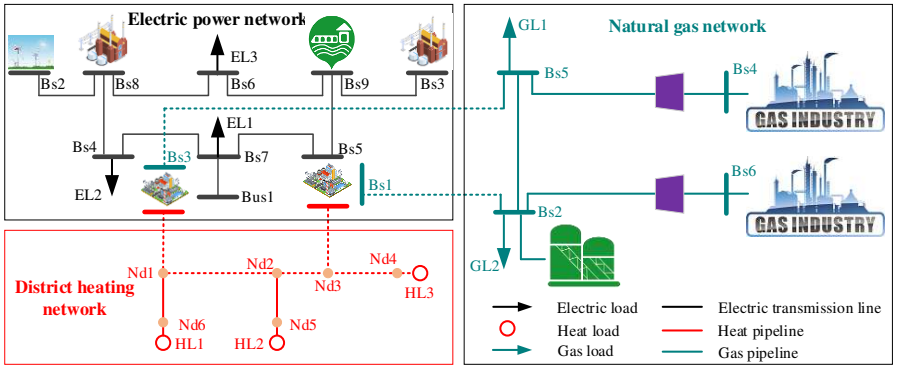

Fig. 5. One-line diagram of the IEGHS.

6.1. Scenarios generation of electricity/heat/gas load

The specific parameters of the generator and discriminator model of GANs are shown in Table 1. The annual electricity/heat/gas load data of a region in Northeast China from 2016 to 2020 are used as historical data samples. The WGANs, GP-WGANs, and GN-WGANs methods are used to generate scenarios, respectively. Fig. 6-Fig. 8 show the training process of generators and discriminators for generating electric load scenarios using three methods. The ordinate "$D(s_r)/D(G(z))$" in Fig. 6- Fig. 8 indicates the output result of the discriminator when the generated sample is $G(z)$. The simulation findings depicted in Fig. 6-Fig. 8 demonstrate that the discriminator can readily differentiate between the generated and real samples during the initial training phase of WGANs, GP-WGANs, and GN-WGANs approaches. With the continuous strengthening of training, they are becoming more and more difficult to distinguish. However, it can be found that the training effect of the method based on GN-WGANs is significantly better than that based on WGANs and GP-WGANs at the later stage of training. The generated samples are so similar to the real samples that it poses a challenge for the discriminator to differentiate between them. That is, the generated data scene can be used as real data as the basis for simulation analysis.

Table 1 The GANs model structure.

	Generator	Discriminator
Input	100	24*24
Layer 1	MLP, 2048	Conv_Layer, 64
Layer 2	MLP, 1024	Conv_Layer, 128
Layer 3	MLP, 128	MLP, 1024
Layer 4	Conv_trans, 128	MLP, 128
Layer 5	Conv_trans, 64	

MLP denotes the multilayer perceptron followed by the number of neurons； Conv_Layer/Conv_trans denotes the convolutional/deconvolutional layers followed by the number of filters. Sigmoid is used to constrain the discriminator's output in [0, 1].

Therefore, this work employs the GN-WGANs method to generate the electricity/heat/gas load demand scenarios and generates 32 power load demand scenarios. Too many scenes will reduce the computational efficiency of the model, while too few scenes will reduce the calculation time, but will reduce the accuracy of the solution. Therefore, IDB determines the minimum number of scenarios in the interval [2, 10] that can balance the solution accuracy and the calculation time.

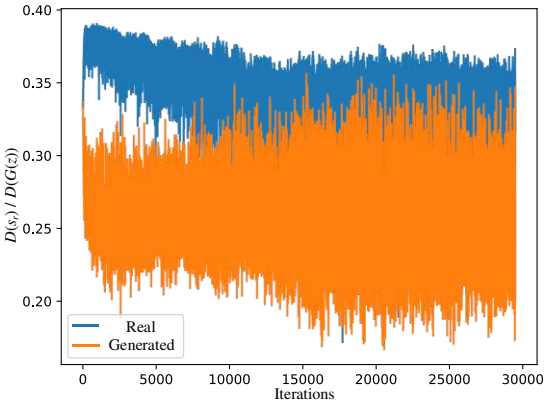

Fig. 6. Training process of the WGANs method.

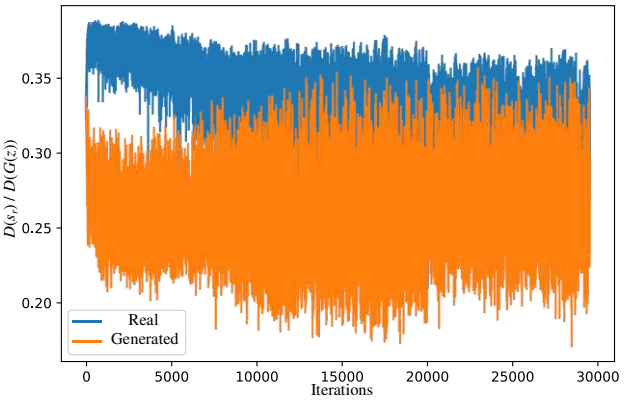

Fig. 7. Training process of the GP-WGANs method.

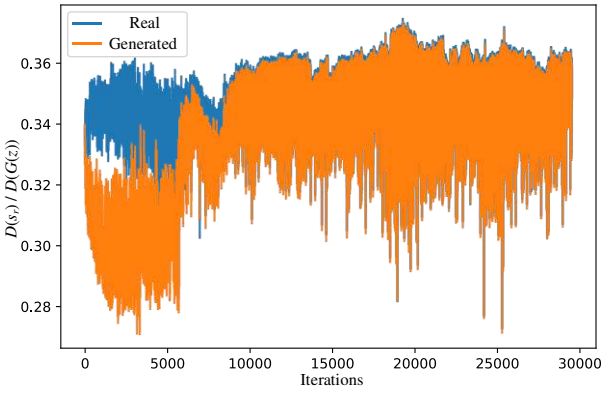

Fig. 8. Training process of the GN-WGANs method.

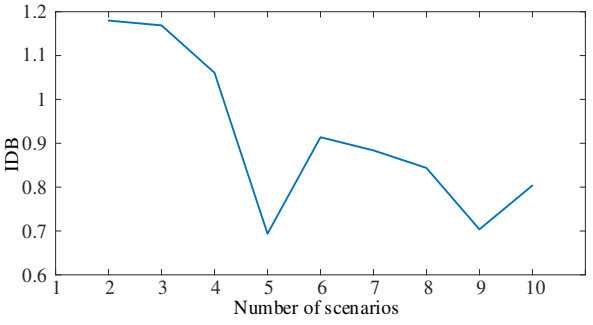

Fig. 9. IDB value of typical scenarios.

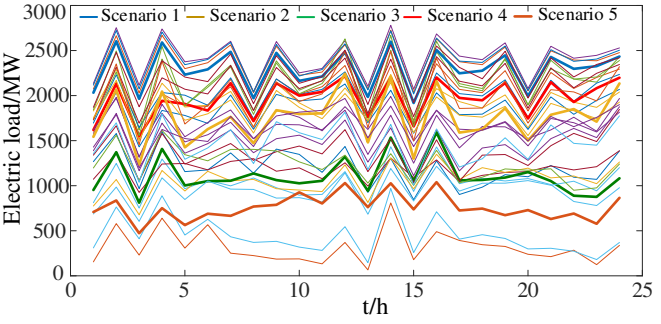

Fig. 10. The electric load scenarios and clustering results.

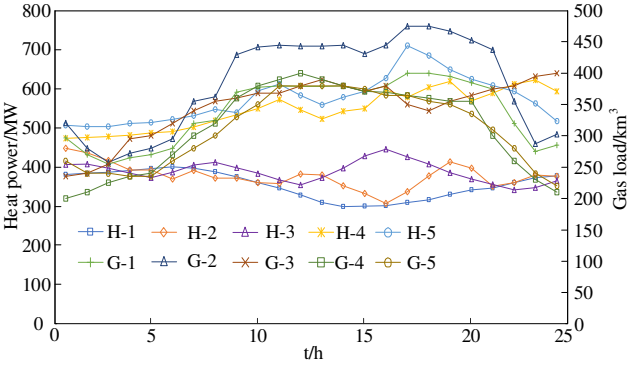

Fig. 11. The curves of heat load and gas load.

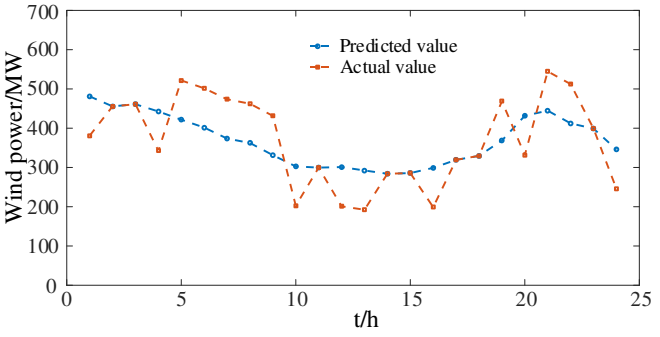

Fig. 12. The predicted and actual curves of wind power.

The IDB value of the number of typical scenes is shown in Fig. 9. The result of Fig. 9 shows that when the number of scenes is 5, the IDB is the lowest. Therefore, the number of clustering centers of the *K*-medoids algorithm is set to 5. The

clustering results are shown by the bold lines in Fig. 10. Based on the same working principle as the typical scenario of generating electrical load demand, the obtained heat-gas load power scenarios are represented in Fig. 11. H-1~H-5 represent typical scenarios of heat load demand 1~5. G-1~G-5 represent typical scenarios of gas load demand 1~5. The curves of wind power are shown in Fig. 12.

6.2. Optimal dispatching results of IEGHS

This example is run on a 2.40 GHz Intel i5-9300h CPU with 16 GB RAM, on a 64-bit operating system. Simulation calculations are performed on Matlab R2016 combined with Cplex 12.5. The ratio of shiftable load α_t^{ELD}, α_t^{HLD} and α_t^{GLD} are 0.1. The budget parameter Γ^{W}=20. This section first verifies the superiority of the proposed improved integrated demand response (IIDR) model and then analyzes the optimization scheduling results of IEGHS. Two cases have been compared:

Case 1: The RSOD model based on IIDR with considering the peak-valley difference cost of the electricity-heat-gas load.

Case 2: The RSOD model based on IDR without considering the peak-valley difference cost of the electricity-heat-gas load.

The two-stage RSOD model is solved, and the optimized load demand curve based on traditional IDR and IIDR is shown in Fig. 13. The optimization results for energy power dispatching were displayed in Figs 14-16. The outcome indicates that IEGHS enables efficient utilization and scheduling of electric, thermal, and natural gas power.

Fig. 13 shows that both the load curves based on IDR and the load curves based on IIDR have a certain impact on the change of electric/gas/thermal load. The load characteristics optimized based on the IDR model will have new load peaks and load valleys, as shown in (a) of Fig. 13. The adjustment effect may be insufficient as shown in (b) and (c) of Fig. 13. Compared with IDR, the IIDR model can improve the load characteristics better and avoid new load peak and valley values. For the given example of electric load, it was observed that the original maximum peak-valley difference was 803.495MW. The maximum peak-valley difference after optimization based on the IDR model is 858.155MW. According to the results of the optimization using the IIDR model, the maximum difference between peak and valley loads is 587.724MW. This represents a 26.85% reduction compared to the original load and a 31.51% reduction compared to the IDR model. These findings confirm that the IIDR model is effective in achieving improved load regulation.

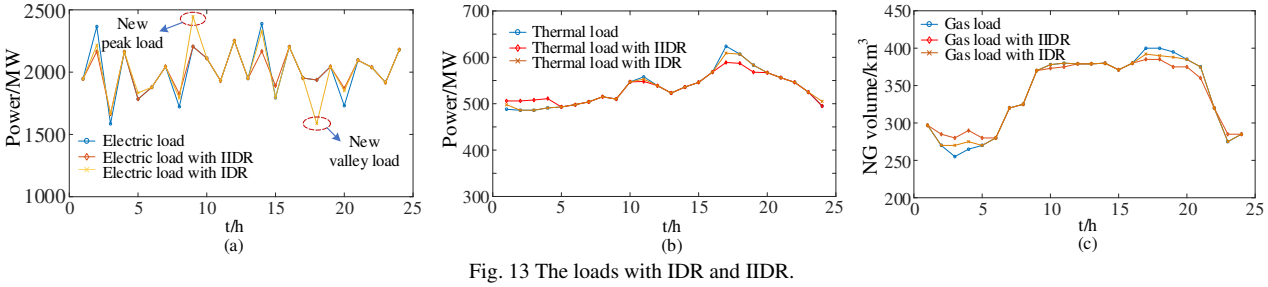

Fig. 13 The loads with IDR and IIDR.

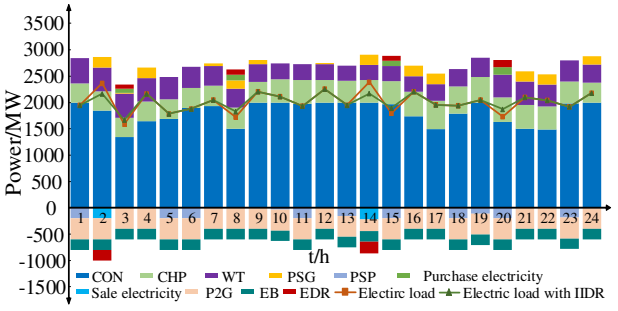

Fig. 14 Electric demand optimization results of IEGHS.

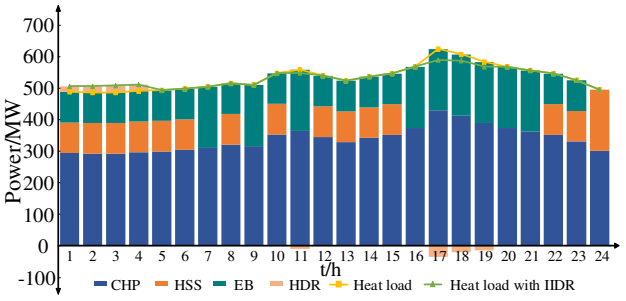

Fig. 15 Thermal demand optimization results of IEGHS.

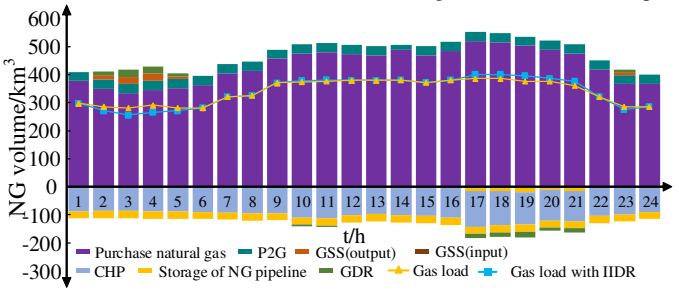

Fig. 16 Gas demand optimization results of IEGHS.

Based on the simulation results displayed in Fig. 14, the CON units and CHP units are in full-time operation to ensure the electric and heat loads. When the wind power is higher than the electric load, P2G equipment, EB equipment, and pumped storage units participate in the operation to absorb more wind power and realize the full utilization of renewable energy. Fig. 15 shows that the CHP unit is the main heating unit. It should be noted that the electric power absorbed by EB from the power grid is mainly converted into direct heating power and heat storage power of the HSS. Fig. 15 does not show the heat absorption power of the HSS, but only shows the heat release power of the HSS. During the peak period 16:00-21:00 of heat load, the direct heating power of EB and CHP units jointly support the heat load. The HSS participates in the operation to reduce the heat supply pressure of the CHP unit and EB at 1:00-6:00 and 24:00.

Fig. 16 shows that the NG demand is mainly supplied by the NG main network, supplemented by the P2G equipment supply. During the valley period of gas load from 2:00-5:00, due to participating in the GDR, the NG demand in the valley period increased, and the GSS started to support the NGN demand. During the peak period of gas load from 17:00-21:00, due to participating in the GDR, the gas load demand was reduced. The GSS started to absorb the transferred gas load demand to achieve cost-effective operation of the NGN in the dispatching period.

Additionally, an analysis is conducted on how various Γ^{W} values affect the system's operational outcomes. A comparison between the presented RSOD model and the results of stochastic and deterministic optimization (DO) is presented in Table 2. The data in Table 2 indicates that as the robust adjustment parameters of WT output power increase, there are more periods during which WT output hits the min and max value within the fluctuation range. This leads to an increase in spinning reserve power after IEGHS dispatching. However, due to the adjustment cost of the IEGHS proposed in this paper being lower than that of the SO model and the DO model, the total operation cost of the RSOD model presented in this work is lower than that of the other two methods. Taking Γ^{W}=16 as an example, the RSOD model presented in this work obtained a total operating cost reduction of 9.29% and 9.35% compared to the SO method and DO method, respectively. The outcome confirms the excellence of the proposed model.

Table 2 Comparison of the total cost for different optimization methods.

		Γ^W				
		0	6	10	16	24
Total cost(10^5\$)	M1	5.64329	5.68987	5.72515	5.78140	5.86907
	M2			6.37346		
	M3			6.37793		

M1 denotes the proposed method in this work. M2 denotes the stochastic optimization method. M3 denotes deterministic optimization.

6.3. Impact of compensation price

This study investigated the impact of different demand response compensation prices on the RSOD issue in IEGHS. Tables 3-5 show the results with Γ^W=16. p_t^{EDRV}, p_t^{HDRV}, p_t^{GDRV} are variable compensation prices. Tables 3-5 show the impact of compensation price changes for IIDR considering only electricity load, only thermal load, and only gas load on system operation results. Based on the data presented in Tables 3-5, it is evident that changing the compensation prices p_t^{EDR}, p_t^{HDR} and p_t^{GDR} will have diverse effects on the functioning outcomes of the operation outcomes of the RSOD model in IEGHS. One of the scenarios that have a major impact on the system operation results is the alteration of the DR compensation price for electricity load. This is because the compensation price for responding to changes in electricity load demand will directly affect the electricity load demand curve, thereby changing the peak-valley difference of the electricity load. Not only will this impact the SR cost of the system, but it will also greatly affect the operating costs of various power supply units for electricity load. In terms of the system operating costs, the effect of altering compensation prices for heat and gas loads is relatively insignificant when compared to the electricity load scenario. One reason is that the heat load is affected by both heat DR and user comfort, and even if the compensation price for heat demand response is increased, the user's enthusiasm will not be high after affecting their comfort. The second reason is that there are fewer types of units for heat load supply and the scale of heat load is relatively small. This second reason also applies to explaining the situation of NGN.

Table 3 Simulation results with varying compensation price p_t^{EDR}.

p_t^{EDRV}/p_t^{EDR}	p_t^{HDRV}/p_t^{HDR} ; p_t^{GDRV}/p_t^{GDR}	Peak-valley difference of electricity load (MW)	Total cost (10^5\$)
0.8	1; 1	677.24	5.8014
0.9	1; 1	632.59	5.7912
1	1; 1	587.72	5.7814
1.1	1; 1	560.78	5.7762
1.2	1; 1	538.29	5.7683

Table 4 Simulation results with varying compensation price p_t^{HDR}.

p_t^{HDRV}/p_t^{HDR}	p_t^{EDRV}/p_t^{EDR} ; p_t^{GDRV}/p_t^{GDR}	Peak-valley difference of heat load (MW)	Total cost (10^5\$)
0.8	1; 1	141.07	5.7872
0.9	1; 1	118.26	5.7844
1	1; 1	96.52	5.7814
1.1	1; 1	84.24	5.7788
1.2	1; 1	76.62	5.7776

Table 5 Simulation results with varying compensation price p_t^{GDR}.

p_t^{GDRV}/p_t^{GDR}	p_t^{EDRV}/p_t^{EDR} ; p_t^{HDRV}/p_t^{HDR}	Peak-valley difference of gas load (km^3)	Total cost (10^5\$)
0.8	1; 1	130.35	5.7864
0.9	1; 1	118.09	5.7841
1	1; 1	105.12	5.7814
1.1	1; 1	94.22	5.7788
1.2	1; 1	85.48	5.7761

6.4. Modified IEEE 118-bus test system

Furthermore, a modified IEEE 118-bus system is carried out to test the validity of the presented RSOD model on large-scale systems. The modified system is made up of 54 generators, 186 transmission lines, and 91 load buses, with 20

of the generators being 100 MW CHP units [42]. Additionally, three wind farms are connected to the system on buses 17, 66, and 94. The DHN consists of 62 nodes and 40 pipelines, including 33 load nodes [14]. The natural gas pipeline consists of 10 nodes and 10 pipelines [40]. Other data and parameters are the same as the modified IEEE 9-bus system. The 118-bus EPN integrated energy system with 62-node DHN and 10-node NGN is shown in Fig. 17. G1~G20 represent the gas load consumed by 20 CHP units in operation, while L1~L6 represent the gas load demand of residents. The case setting is consistent with the modified 9-bus test system.

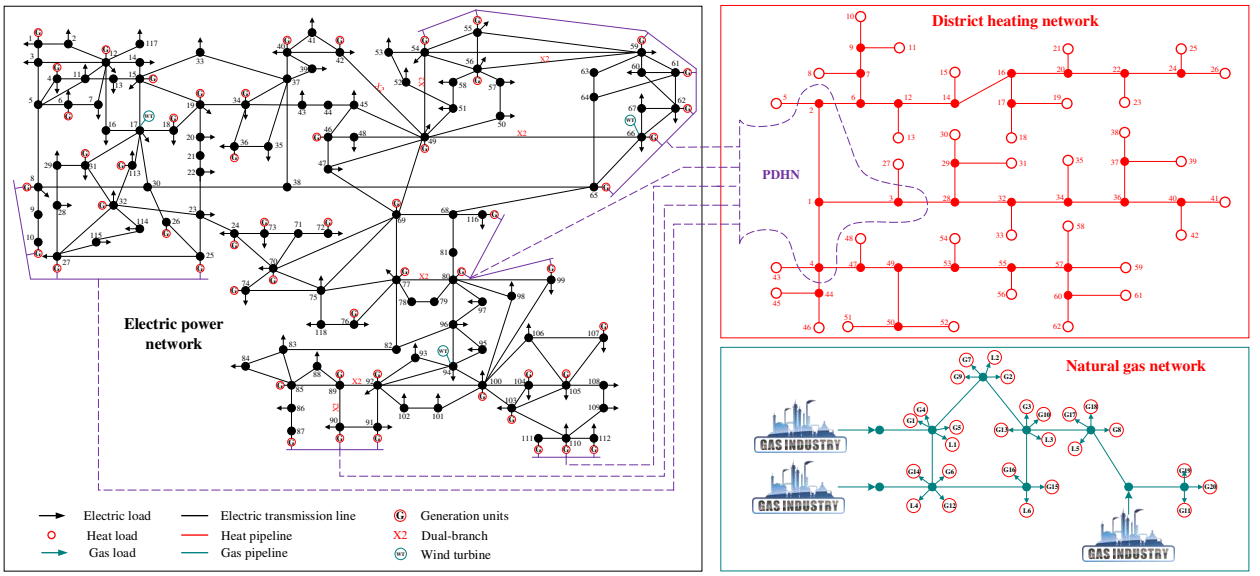

Fig. 17 118-bus EPN integrated system with 62-node DHN and 10-node NGN.

The comparison of dispatching results for different cases is shown in Table 6. Based on the scheduling results obtained in Case 1, Table 6 shows that the difference between peak and valley loads for electricity, heat, and gas is smaller than in Case 2. At Γ^{W}=16, taking the electric load scenario as an example, the peak-valley difference of the optimized electric load in Case 1 is 405.96 MW, which is 29.69% lower than the optimized result in Case 2. Meanwhile, due to the small peak-valley difference of Case 1, the total SR cost of the system will be lower than Case 2. Therefore, although the peak-valley difference cost of Case 1 is relatively higher than that of Case 2, it is much smaller compared with the increased system SR cost. Therefore, the total operating cost based on Case 1 is lower than Case 2. The validity and superiority of the proposed model are verified.

Table 6 Comparison of scheduling results for different cases.

		Peak-valley difference			Total cost /10^7\$
		Electricity load (MW)	Heat load (MW)	Gas load (km^3)	
Case1	Γ^{W}=10	352.89	152.76	732.18	2.8319
	Γ^{W}=16	405.96	175.92	775.62	2.8350
Case2	Γ^{W}=10	524.39	188.48	824.56	2.8431
	Γ^{W}=16	577.36	207.26	857.38	2.8463

7. Conclusion

In this paper, the modeling of generation and load uncertainty and demand side response in IEGHS are studied, and an RSOD model of an IEGHS considering improved IDR is established. The effectiveness and superiority of this method are verified by the examples. The conclusions are as follows:

1) The RSOD approach proposed can achieve cost-effective scheduling of every unit within the IEGHS to fulfill the

demands of multi-energy loads even in the worst-case scenario.

2) Compared with WGANs and GP-WGANs methods, the GN-WGANs method has better training performance and can generate more accurate load scenarios.

3) The improved IDR model can better adjust the load characteristics and avoid excessive or insufficient DR.

4) The modified IEEE 9-bus system and IEEE-118 bus system are simulated, and consistent simulation results are obtained. At the same time, the compromise between the economy and the robustness of the model can be achieved by adjusting the budget parameters.

It should be noted that this paper only studies the optimization dispatching model of IEGHS considering integrated demand response to address the uncertainty of wind power and load demand, providing a new approach for optimization dispatching of IEGHS considering demand response. However, the IEGHS optimization dispatching model studied in this article without considering the uncertainty factors in the operation of regional heat and natural gas networks. This is also the next research work to be carried out in this article to continuously improve the research on IEGHS uncertainty scheduling.

References

[1] Kong X, Xiao J, Liu D, Wu J, Wang C, Shen Y. Robust stochastic optimal dispatching method of multi-energy virtual power plant considering multiple uncertainties. Appl Energy 2020;279:1-13.

[2] Cheng Y, Zhang N, Wang Y, Yang J, Kang C, Xia Q. Modeling carbon emission flow in multiple energy systems. IEEE Trans Smart Grid 2019;10(4):3562-74.

[3] Li X, Zhang R, Bai L, Li G, Jiang T, Chen H. Stochastic low-carbon scheduling with carbon capture power plants and coupon-based demand response. Appl Energy 2018;210:1219-28.

[4] Zhang Z, Sun Y, Gao D, Lin J, Cheng L. A versatile probability distribution model for wind power forecast errors and its application in economic dispatch. IEEE Trans Power Syst 2013;28(3):3114-25.

[5] Huo D, Gu C, Ma K, Wei W, Xiang Y, Blond SL. Chance-constrained optimization for multi energy hub systems in a smart city. IEEE Trans Ind Electron 2019;66(2):1402-12.

[6] Moazeni S, Miragha AH, Defourny B. A risk-averse stochastic dynamic programming approach to energy hub optimal dispatch. IEEE Trans Power Syst 2019;34(3):2169-78.

[7] Zhang R, et al. Adjustable robust power dispatch with combined wind-storage system and carbon capture power plants under low-carbon economy. Int J Electr Power Energy Syst 2019;113:772-81.

[8] Lu X, Liu Z, Li M, Wang L, Zhou K, Feng N. A robust optimization approach for optimal load dispatch of community energy hub. Appl Energy 2020;259:114195.1-114195.13.

[9] Rooks C, et al. Robust hierarchical dispatch for residential distribution network management considering home thermal flexibility and model predictive control. IET Gener Transm Distrib 2021;15:2567-81.

[10] Chang XY, Xu YL, Gu W, Sun HB, Chow MY, Yi ZK. Accelerated distributed hybrid stochastic/robust energy management of smart grids. IEEE Trans Ind Informat 2021;17(8):5335-47.

[11] Chang XY, Xu YL, Sun HB. Vertex scenario-based robust peer-to-peer transactive energy trading in distribution networks. Int J Electr Power Energy Syst 2022;138:107903.1-107903.11.

[12] Nikoobakht A, Aghaei J, Massrur HR, Hemmati R. Decentralised hybrid robust/stochastic expansion planning in coordinated transmission and active distribution networks for hosting large-scale wind energy. IET Gener Transmiss Distrib 2020;14(5):797-807.

[13] Li Y, Han M, Shahidehpour M, Li JZ, Long C. Data-driven distributionally robust scheduling of community integrated energy systems with uncertain renewable generations considering integrated demand response. Appl Energy Apr. 2023;335:120749.1-120749.17.

[14] Tan H, Yan W, Ren Z, Wang Q, Mohamed MA. A robust dispatch model for integrated electricity and heat networks considering price-based integrated demand response. Energy 2022;239:121875-86.

[15] Li Y, Wang B, Yang Z, Li JZ, Li GQ. Optimal scheduling of integrated demand response-enabled community-integrated energy systems in uncertain environments. IEEE Trans Industry Applications Apr. 2022;58(2):2640-51.

[16] Ni L, et al. Optimal operation of electricity, natural gas and heat systems considering integrated demand responses and diversified storage devices. J Mod Power Syst. Clean Energy 2018;6(3):423-37.

[17] Lu J, Liu TQ, He C, Lu N, Hu XT. Robust day-ahead coordinated scheduling of multi-energy systems with integrated heat-electricity demand response and high penetration of renewable energy. Renew Energy 2021;178:466-82.

[18] He L, Lu Z, Geng L, Zhang J, Li X, Guo X. Environmental economic dispatch of integrated regional energy system considering integrated demand response. Int J Electr Power Energy Syst 2020;116:105525-38.

[19] Liu G, Xu Y, Tomsovic K. Bidding strategy for microgrid in day-ahead market based on hybrid stochastic/robust optimization. IEEE Trans Smart Grid 2016;7:227-37.

[20] Wang J, Zhong H, Tang W, Rajagopal R, Xia Q, Kang C. Optimal bidding strategy for microgrids in joint energy and ancillary service markets considering flexible ramping products. Appl Energy 2017;205:294-303.

[21] Wang S, Chen H, Pan Z, Wang J. A reconstruction method for missing data in power system measurement using an improved generative adversarial network. CSEE J of Power Energy Syst 2019;39:56-64.

[22] Dai Y, et al. Dispatch model for CHP with pipeline and building thermal energy storage considering heat transfer process. IEEE Trans Sustain Energy 2019;10(1):192-203.
[23] Lin C, Wu W, Zhang B, Sun Y. Decentralized solution for combined heat and power dispatch through benders decomposition. IEEE Trans Sustain Energy 2017;8(4):1361-72.
[24] Correa-Posada CM, Sánchez-Martín P. Integrated power and natural gas model for energy adequacy in short-term operation. IEEE Trans Power Syst 2015;30(6):3347-55.
[25] Khani H, Farag HEZ. Optimal day-ahead scheduling of power-to-gas energy storage and gas load management in wholesale electricity and gas markets. IEEE Trans Sustain Energy 2018;9(2):940-51.
[26] Yang X, Chen Z, Huang X, Li R, Xu S. Robust capacity optimization methods for integrated energy systems considering demand response and thermal comfort. Energy 2021;221:119727-40.
[27] Sheng S, Zhang L. Economic dispatch of power system considering the prediction error of wind power, solar energy and load. Proc CSU-EPSA 2017;29(9):80-85.
[28] Miyato T, Kataoka T, Koyama M, Yoshida Y. Spectral normalization for generative adversarial networks. In International Conference on Learning Representations, Vancouver, Canada: Ithaca, NY: arXiv.org 2018:1-26.
[29] Wu Y, Shuai H, Tam Z, Chiu H. Gradient normalization for generative adversarial networks. IEEE International Conference on Computer Vision, Canada: Montreal, IEEE 2021:1-23.
[30] Thanh-Tung H, Tran T, Venkatesh S. Improving generalization and stability of generative adversarial networks. In International Conference on Learning Representations 2019:1-18.
[31] Gulrajani I, Ahmed F, Arjovsky M, Dumoulin V, Courville A. Improved training of wasserstein gans. In Proceedings of the 31st International Conference on Neural Information Processing Systems, Long Beach, CA, USA: NIPS 2017:5769-79.
[32] Jiang C, Mao Y, Chai Y. Day-ahead renewable scenario forecasts based on generative adversarial networks. Int J Energy Res 2021;45:7572-87.
[33] Wang Q, Dong W, Yang L. A wind power/photovoltaic typical scenario set generation algorithm based on Wasserstein distance metric and revised K-medoids cluster. CSEE J Power Energy Syst 2015;35:2654-61.
[34] Yu D, Liu G, Guo M, Liu X. An improved K-medoids algorithm based on step increasing and optimizing medoids. Expert Systems with Application 2018;92:464-73.
[35] Li R, Wang W, Wu X, Tang F, Chen Z. Cooperative planning model of renewable energy sources and energy storage units in active distribution systems: A bi-level model and pareto analysis. Energy 2019;168:30-42.
[36] Shui Yue, Liu Junyong, Gao Hongjun, Huang Shan, Jiang Zhuozhen. A distributionally robust coordinated dispatch model for integrated electricity and heating systems considering uncertainty of wind power. Proceedings of the CSEE, 2018;38(24):7235-7247.
[37] Dai CX, Wu L, Wu HY. A multi-band uncertainty set based robust SCUC with spatial and temporal budget constraints. IEEE Trans Power Syst 2016;31(6):4988-5000.
[38] Zeng B, Zhao L. Solving two-stage robust optimization problems using a column-and-constraint generation method. Oper Res Lett 2013;41(5):457-61.
[39] An Y, Zeng B. Exploring the modeling capacity of two-stage robust optimization: variants of robust unit commitment model. IEEE Trans Power Syst 2014;30(1):109-22.
[40] Alabdulwahab A, Abusorrah A, Zhang X, Shahidehpour M. Stochastic security-constrained scheduling of coordinated electricity and natural gas infrastructures. IEEE Syst J 2017;11(3):1-10.
[41] Li J, Fang J, Zeng Q, Chen Z. Optimal operation of the integrated electrical and heating systems to accommodate the intermittent renewable sources. Appl Energy 2016;167:244-54.
[42] Yang M, Wang M, Cheng F, Lee WJ. Robust economic dispatch considering automatic generation control with affine recourse process. Int J Electr Power Energy Syst 2016;81:289-98.